




In situ construction of graded porous carbon matrix to strengthen structural stability of NiFe₂O₄ nanoparticles as high-capacity anodes of Li-ion batteries

Taolin Zhao^{1,2,3,*} , Xiyun Huang¹, Yu Meng¹, Jiangang Shen¹, Yingdi Zheng¹, Liyao Chang¹, and Shaokang Chen¹

¹School of Materials Science and Engineering, Shijiazhuang Tiedao University, Shijiazhuang 050043, China

²Hebei Key Laboratory of Advanced Materials for Transportation Engineering and Environment, Shijiazhuang 050043, China

³Hebei Engineering Research Center of Metamaterials and Micro-Devices, Shijiazhuang 050043, China

Received: 19 February 2022

Accepted: 21 July 2022

Published online:

8 August 2022

© The Author(s), under exclusive licence to Springer Science+Business Media, LLC, part of Springer Nature 2022

ABSTRACT

Transition metal oxides are considered as promising anode materials of high-performance lithium-ion batteries because of their higher specific capacities than that of commercial graphite. However, they still suffer from huge volume expansion/contraction during cycling, leading to fast decay of the reversible capacity and poor cycle stability. In this work, a graded porous carbon matrix has been in situ constructed successfully to strengthen structural stability of NiFe₂O₄ nanoparticles via a facile and green low-temperature combustion method. The calcination temperature has a significant effect on the purity and electrochemical performances of the final NiFe₂O₄/C composites. NiFe₂O₄/C prepared at 350 °C shows a high first discharge capacity of 1385.8 mAh g⁻¹ at 200 mA g⁻¹, excellent cycle stability, and good rate capability. This excellent electrochemical performance may be attributed to its favorable graded porous structure. The carbon matrix can effectively protect the NiFe₂O₄ nanoparticles, buffer the surface stress caused by volume expansion/contraction, and facilitate the transmission of electrons and Li⁺ ions. The symbiotic relationship between NiFe₂O₄ active nanoparticles and graded porous carbon matrix strengthens the structural stability of the electrode, which expands the way of designing high-performance electrode materials for secondary rechargeable batteries.

Handling Editor: Mark Bissett.

Address correspondence to E-mail: zhaotl@stdu.edu.cn

<https://doi.org/10.1007/s10853-022-07576-z>

Introduction

Since the Industrial Revolution, the booming development of oil, coal, and other resources has promoted the great development of the world economy, but also brought an unbearable burden to the environment. Therefore, it is urgent to develop new renewable clean energy and energy storage system [1–5]. Nowadays, Li-ion batteries (LIBs) have become the main driving force in almost all aspects of human life and production [6–9]. However, with the increase in battery market demand, the development of electrode materials with higher capacity and better safety has become the focus of realizing high-performance LIBs in the future [10–15].

As promising alternative anodes of traditional low-capacity graphite material (372 mAh g^{-1}) [16, 17], transition metal oxides with high theoretical specific capacity have gained extensive attention [18–23]. Among them, NiFe_2O_4 (915 mAh g^{-1}) with an inverse spinel structure has been widely studied [24–26] because of the abundance of Fe and Ni elements in the earth, its relatively low toxicity, the possibility of inserting more Li^+ ions and, in particular, its high initial discharge capacity. However, the poor electrical conductivity and severe volume expansion/contraction upon cycling result in severe capacity decay, which has limited its practical application [27].

To solve the above issues, many researchers have conducted a lot of research in the design of various nanostructured NiFe_2O_4 or the formation of composites with carbon materials [26, 28–30]. Nanostructure can increase the specific surface area and the interfacial area between electrolyte and electrode, thus providing numerous active sites for electrochemical reactions. High-conductive carbon materials can significantly improve the electronic conductivity and buffer the volume expansion of the metal oxide material. For example, Lei et al. designed heterostructured $\text{NiFe}_2\text{O}_4/\text{C}$ nanorods via a wet chemical method. The obtained composite delivered a high reversible capacity as high as 650.2 mAh g^{-1} even at a high current density of 2 A g^{-1} after 500 cycles [27]. Jin et al. fabricated hierarchical mesoporous $\text{NiFe}_2\text{O}_4/\text{C}$ hollow spheres by a hydrothermal method and sintering treatment. This composite exhibited a reversible capacity of 633.3 mAh g^{-1} at 10 A g^{-1} after 250 cycles [31]. Zhang et al. prepared

$\text{NiFe}_2\text{O}_4\text{-rGO}$ nanocomposite through a facile hydrothermal method, which showed excellent cycling stability and a high specific capacity of 1129 mAh g^{-1} at 0.2 A g^{-1} [32]. Zou et al. designed $\text{NiFe}_2\text{O}_4/\text{CNTs}$ with a coaxial structure, which depicted a high reversible capacity of 250 mAh g^{-1} at a high current density of 2 A g^{-1} after 100 cycles [30].

By combining NiFe_2O_4 with carbon materials, the composite materials with special spatial structure can show significantly improved electrochemical performance. Herein, in order to improve the low conductivity and the volume change during cycling of NiFe_2O_4 , a graded porous carbon matrix encapsulated nano- NiFe_2O_4 particles has been in situ constructed via a facile low-temperature combustion method to strengthen the structural stability of $\text{NiFe}_2\text{O}_4/\text{C}$ composites. NiFe_2O_4 nanoparticles and porous carbon matrix can be formed instantaneously after calcining the mixture of gelatin and metal nitrates. The structure, morphology, and electrochemical properties of the composites prepared at different calcination temperatures are further investigated. $\text{NiFe}_2\text{O}_4/\text{C}$ composite calcined at $350 \text{ }^\circ\text{C}$ exhibits excellent cycle stability and rate performance. The unique graded porous structure of the composite materials can provide a high specific surface area, more reactive sites and increased diffusion mobility of electrons and Li^+ ions.

Experimental section

Material synthesis

The synthesis process of the graded porous $\text{NiFe}_2\text{O}_4/\text{C}$ composites is shown in Fig. 1a. $\text{Fe}(\text{NO}_3)_3 \cdot 9\text{H}_2\text{O}$ (2.694 g) and $\text{Ni}(\text{NO}_3)_2 \cdot 6\text{H}_2\text{O}$ (0.968 g) were dissolved in deionized water (40 mL) under magnetic stirring for 0.5 h . Gelatin (10 g) was dissolved in deionized water (90 mL) under stirring for 1 h at $60 \text{ }^\circ\text{C}$ to form a homogeneous gelatin solution. Then, the bimetallic salt solution was pumped to gelatin solution (20 mL) by a peristaltic pump to obtain a uniform solution. The mixed solution became a viscous syrup gel gradually through continuous magnetic stirring and evaporating in a water bath. Subsequently, the gel was dried in a vacuum drying oven at $80 \text{ }^\circ\text{C}$ to obtain a porous and fluffy precursor. Finally, the precursor was placed in a tube furnace filled with argon and calcined at various

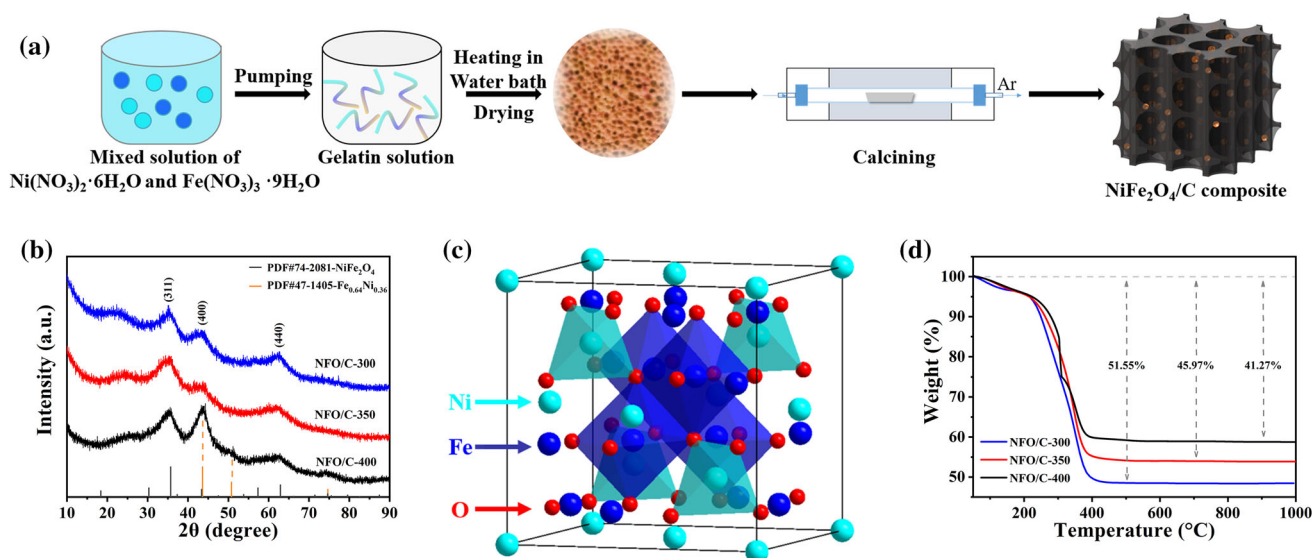


Figure 1 a Synthesis process of $\text{NiFe}_2\text{O}_4/\text{C}$, b XRD patterns of all the materials, c crystal structure of NiFe_2O_4 , and d TG curves of all the materials.

temperatures. The $\text{NiFe}_2\text{O}_4/\text{C}$ products obtained at 300 °C, 350 °C, and 400 °C were named NFO/C-300, NFO/C-350, and NFO/C-400, respectively.

Material characterizations

The crystal composition of the prepared samples was characterized using D8AD VANCE powder X-ray diffraction (XRD) in the 2θ range of 10–90° with a scan rate of 0.2 s step^{-1} . The morphologies and structures of the fabricated samples were characterized by scanning electron microscopy (SEM, SU8010) and transmission electron microscopy (TEM, JEM-2010). Thermogravimetry (TG) analysis of the samples was conducted on a thermogravimetric analyzer (Mettler Toledo TGA/DSC³⁺) at a heating rate of 10 °C min^{-1} from 50 to 1000 °C under air atmosphere. Nitrogen adsorption/desorption isotherms were performed on a Micromeritics-Instrument (ASAP-2020, Micromeritics, USA). The specific surface area was calculated according to the Brunauer–Emmett–Teller (BET) method. Raman spectroscopy was carried out on a Horiba LabRAM HR Evolution with 633 nm excitation laser wave length. High-resolution transmission electron microscopy (HRTEM), selected area electron diffraction (SAED), and elemental mapping images (EDS) were characterized on field-emission transmission electron microscopy (FETEM, JEM-2100 F).

Electrochemical measurements

Sodium carboxymethyl cellulose (CMC), acetylene black, and the prepared active material were mixed at a weight ratio of 1:1:8 with deionized water as solvent and grounded evenly in an agate mortar. Then, the homogeneous slurry was uniformly pasted onto the Cu current collector and dried at 80 °C in a vacuum oven. The processed foil was cut into several disks with a diameter of 11 mm. The mass loading of the active materials in a circular electrode was about 2 mg cm^{-2} . The electrochemical measurements of $\text{NiFe}_2\text{O}_4/\text{C}$ were performed on coin cells (CR 2025) assembled in a glove box filled with argon. The prepared circular electrode sheet was used as working electrode. The counter electrode was lithium metal foil and the separator was Celgard 2400. The electrolyte was 1 mol L^{-1} LiPF_6 dissolved in the mixed solvent of diethyl carbonate (DEC) and ethylene carbonate (EC) (1:1 in volume). The galvanostatic charge–discharge tests were performed on a battery tester (LAND CT2001A, Wuhan, China) in the voltage range of 0.005–3.0 V at 25 °C. Cyclic voltammetry (CV) tests were performed by using an electrochemical workstation (CHI660E, Shanghai, China) in the potential range from 0.005 to 3.0 V. The electrochemical impedance spectroscopy (EIS) was also conducted on the electrochemical workstation in a frequency range from 0.01 Hz to 100 kHz.

Results and discussion

Structural characterization

XRD patterns of the NiFe₂O₄/C materials are shown in Fig. 1b. The main diffraction peaks of NFO/C-300 and NFO/C-350 both correspond to the standard diffraction peaks of NiFe₂O₄. The inverse spinel structure (Fd- $\bar{3}m$ space group) of NiFe₂O₄ is illustrated in Fig. 1c. In the structure, O forms face-centered cubic packing with Fe³⁺ ions occupying octahedral and tetrahedral sites, whereas Ni²⁺ cation only occupies the octahedral sites. With such a structure, it can provide surface redox-active metal centers for activating electro-active substances [33]. The diffraction peaks of NiFe₂O₄ can also be observed in NFO/C-400. Besides, some distinct diffraction peaks corresponding to Fe_{0.64}Ni_{0.36} are found at 43.6°, 50.8°, and 74.7°, which may be derived from the reduction of NiFe₂O₄ in NFO/C-400. The diffraction peaks of all the materials are broad with low intensity, indicating that the NiFe₂O₄ grains in the obtained materials have a low crystallinity due to the low-temperature calcination. In addition, the broad diffraction peaks from 20° to 30° in the XRD patterns of the three samples can be attributed to carbon material, which matches well with previous reports [34]. In the XRD patterns, the high background suggests that the carbon in the materials may be in the form of amorphous carbon [35]. No additional impurity peaks are observed, indicating that NiFe₂O₄/C can be successfully prepared by the low-temperature combustion method in this work. Raman spectroscopy was carried out to further investigate the characteristics of carbon in NiFe₂O₄/C materials, as shown in Fig. S1. In the three samples, two distinct peaks at about 1354 cm⁻¹ and 1572 cm⁻¹ correspond to the defect-induced (D) mode and graphenic-induced (G) mode of amorphous carbon [36], respectively. The peak intensity ratios (I_D/I_G) of D band to G band of NFO/C-300, NFO/C-350, and NFO/C-400 are estimated to be about 0.97, 0.96, and 0.95, respectively, indicating that the carbon species in NiFe₂O₄/C materials are partially graphitized, which is beneficial to enhance the conductivity of composites [18].

To estimate the carbon content in the NiFe₂O₄/C composites, TG tests were carried out on NiFe₂O₄/C materials and the results are shown in Fig. 1d. Below 200 °C, a slight weight loss can be observed, which

may be attributed to a small amount of water molecules adsorbed on the particle surface [37]. All three materials present significant mass loss in the temperature range of 200–400 °C, which is ascribed to the oxidation of carbon [21]. The weight loss for NFO/C-300, NFO/C-350, and NFO/C-400 are 51.55%, 45.97%, and 41.27%, respectively. The appropriate carbon content in the composite is conducive to improving the transfer speed of ions and electrons inside the composite and buffering the volume expansion/contraction phenomenon of the metal oxide particles during cycling to some extent.

Morphological and structural analyses

SEM images of NFO/C-300, NFO/C-350, and NFO/C-400 are exhibited in Fig. 2. As can be seen in Fig. 2a–c, all the samples show a continuous network-like porous structure, which is caused by the formation of gas bubbles due to the reaction of gelatin with nitrate [34]. Obviously, the pore diameters of all samples basically belong to macropores, which are good for the rapid infiltration of the electrolyte into the interior of the composites, making the electrolyte fully in contact with the electrode material. In Fig. 2d–f, the surface of the pores is smooth and the wall thickness is between 100 and 200 nm. No obvious particles can be observed, possibly because the grains are too small due to the low calcination temperature. Furthermore, the surface morphology of the composites does not change obviously with the change of calcination temperature.

The microscopic morphology of the NiFe₂O₄/C material can be further observed from TEM images. As shown in Fig. 3a–c, a plurality of holes with different sizes is connected into lamellar amorphous carbon. In Fig. 3d–f, nano-sized NiFe₂O₄ particles are homogeneously embedded inside the carbon matrix. With the increase in calcination temperature, NiFe₂O₄ nanoparticles become more visible, indicating that the particle size gradually increases. The formation of nano-sized particles is related to the low calcination temperature. Nano-active materials are helpful to shorten the transport path of Li⁺ ions and electrons in the solid phase, so as to promote the specific capacity and enhance the rate performance. In addition, the carbon matrix surrounded the surface of nanoparticles can effectively avoid particle agglomeration and protect the metal oxide particles. Fig. S2 shows the HRTEM and SAED images of the NFO/C-350

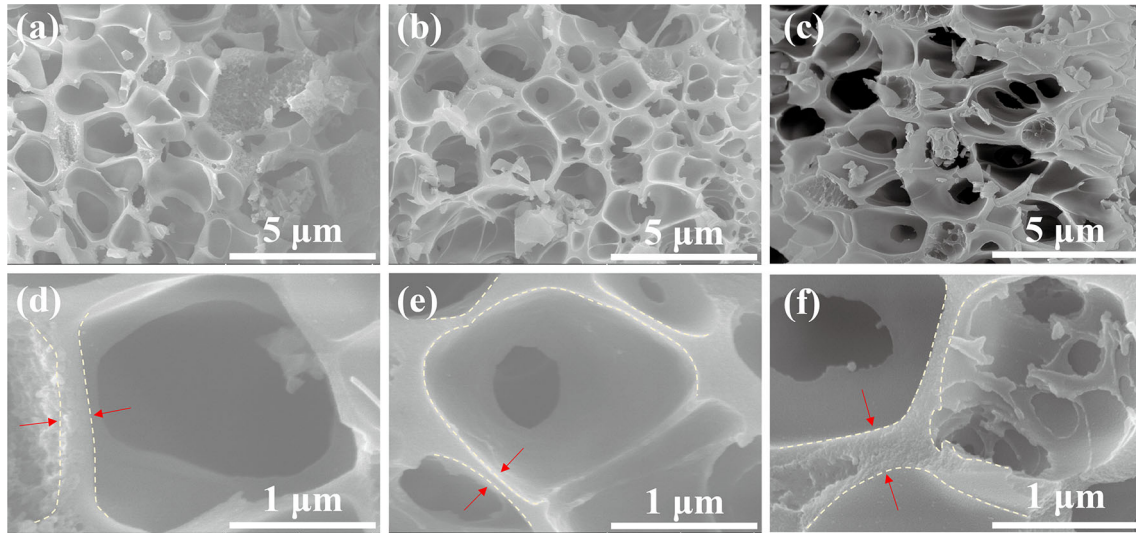


Figure 2 SEM images of **a, d** NFO/C-300, **b, e** NFO/C-350, and **c, f** NFO/C-400.

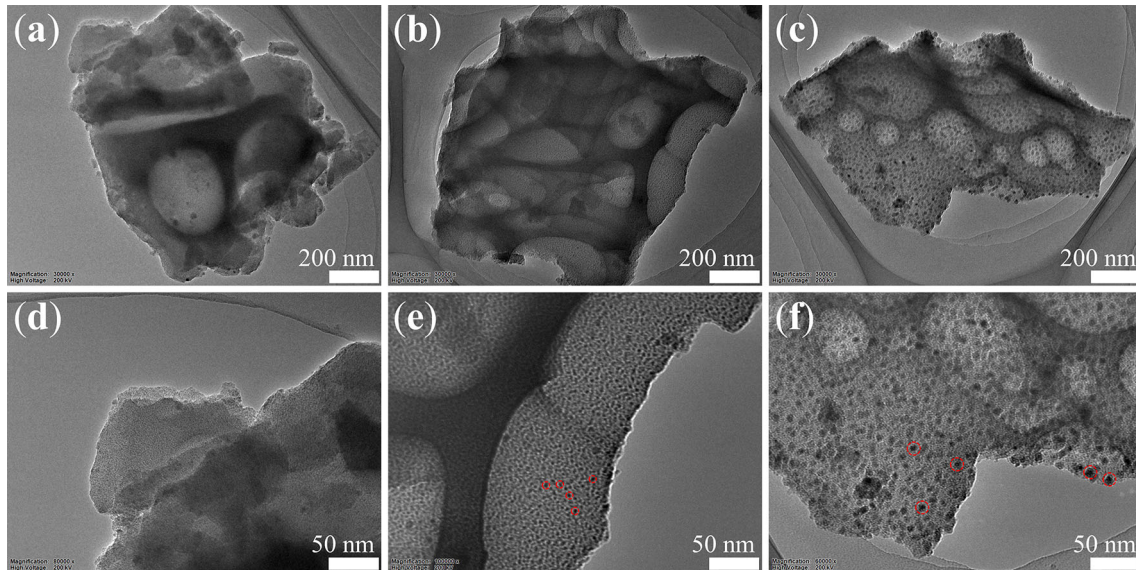


Figure 3 TEM images of **a, d** NFO/C-300, **b, e** NFO/C-350, and **c, f** NFO/C-400.

composite. As shown in Fig. S2a, NiFe_2O_4 particles show clear lattice fringes with interplanar spacing of 0.21 nm, which correspond to the (4 0 0) crystalline plane of NiFe_2O_4 [38]. A series of diffraction rings present in the SAED image in Fig. S2b indicate the polycrystalline nature of NiFe_2O_4 [39], which matches well with the XRD analysis. As shown in Fig. S3, the EDS elemental mapping images of NFO/C-350 indicate the coexistence and uniform distribution of Fe, Ni, O, C, and N elements. The existence of nitrogen may be due to the residual N species from thermal decomposition of gelatin. Nitrogen atoms tend to form covalent bonds with carbon atoms.

Doping nitrogen atoms can enhance the local activity of carbon, thus enhancing the conductivity of the carbon matrix [34]. Therefore, the existence of N species may help to improve the electrochemical properties of composites.

The porous nature of the $\text{NiFe}_2\text{O}_4/\text{C}$ composites can be determined by N_2 adsorption/desorption isotherms and pore size distribution curves. As can be seen in Fig. 4a–c, the N_2 adsorption/desorption isotherm exhibits a typical type-IV curve and a clear H3 type hysteresis loop at high relative pressure (P/P_0), indicating the presence of mesopores contributed by the carbon matrix [18]. The specific surface areas

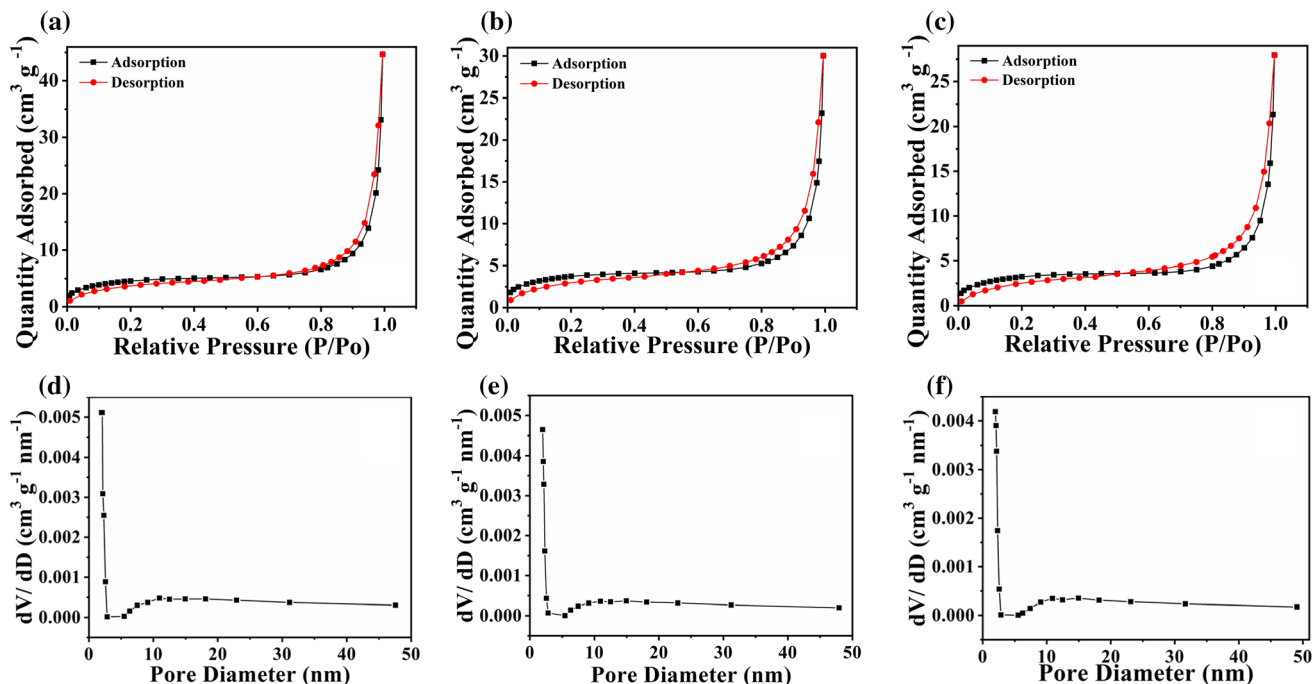


Figure 4 N_2 adsorption/desorption isotherm and the corresponding pore size distribution of **a, d** NFO/C-300, **b, e** NFO/C-350, and **c, f** NFO/C-400.

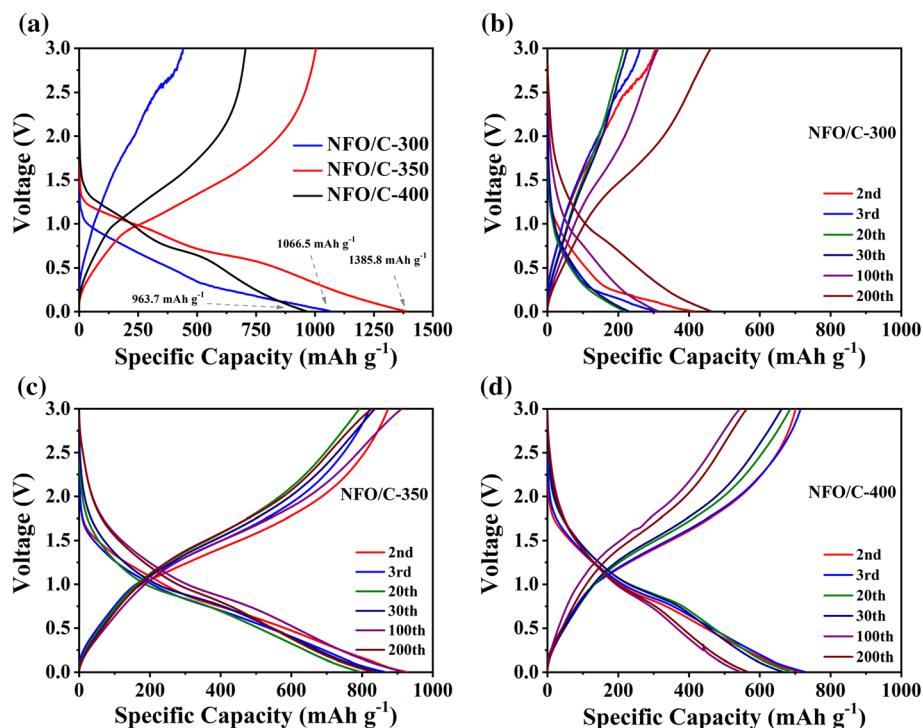
of NFO/C-300, NFO/C-350, and NFO/C-400 are 16.7958, 13.7135, and 12.0402 $m^2 g^{-1}$, respectively. The specific surface area of the material decreases with the increase in calcination temperature, which is related to the decrease in the carbon content in the material. The pore size distribution curves in Fig. 4d–f show that the mesopore size in the $NiFe_2O_4/C$ composites prepared at different calcination temperatures does not differ significantly. The average mesopore sizes of NFO/C-300, NFO/C-350, and NFO/C-400 are 7.4146 nm, 6.7135 nm, and 6.9602 nm, respectively. The existence of mesopores is beneficial to increase the specific surface area and increase the interfacial contact area between electrolyte and electrode as well as provide more reactive sites. Besides, the mesoporous structure may form three-dimensional pore channels inside the material, which is beneficial for the diffusion of electrolyte, electrons and Li^+ ions. Together with the results of SEM and TEM, it can be seen that both mesopores and macropores are present in the composites, indicating the formation of graded porous structure. The simultaneous existence of macropores and mesopores facilitates the gradual infiltration of electrolytes into the interior of the composite. In addition, the graded porous structure can effectively buffer the

volume expansion/contraction during the intercalation/deintercalation of Li^+ ions.

Electrochemical performance

Figure 5 shows the charge/discharge curves of the $NiFe_2O_4/C$ materials at a current density of 200 $mA g^{-1}$. All three samples show typical charge/discharge curves of the metal oxide materials. During the first cycle, the active material consumes part of active lithium to react with the electrolyte for forming a solid electrolyte interphase (SEI) film on the electrode surface [40]. In Fig. 5a, the plateaus in the first discharge process correspond to the formation of the SEI film and the conversion of a small amount of $NiFe_2O_4$ into Ni and Fe metallic nanocrystals through redox reactions [41, 42]. The discharge voltage gradually decreases as the calcination temperature decreases, because the excessive carbon content is not conducive to the effective interfacial contact between the $NiFe_2O_4$ active particles and the electrolyte. When the carbon content is too high, Li^+ ions need to pass through the thick carbon wall to participate in the electrochemical reaction with the $NiFe_2O_4$ nanoparticles inside the carbon matrix, resulting in a certain hysteresis in the reaction potential.

Figure 5 Charge/discharge curves of the **a** first cycle and **b–d** selected cycles of all the samples.



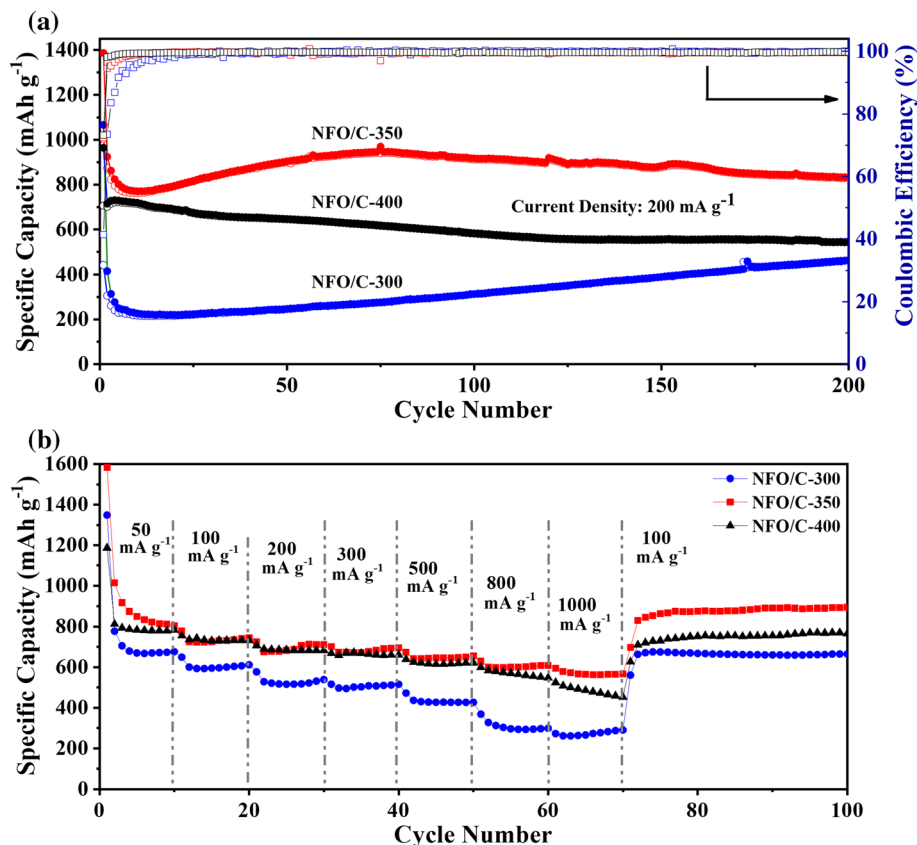
The first discharge specific capacities of NFO/C-300, NFO/C-350, and NFO/C-400 are 1066.5, 1385.8, and 963.7 mAh g⁻¹, respectively. The corresponding initial Coulombic efficiencies are 41.4%, 72.5%, and 73.2%, respectively. The significant capacity loss at the first cycle is related to the irreversible decomposition of the SEI film and incomplete conversion reaction [36, 43]. SEI film growth, as the main side reaction of lithium ion batteries at anode/electrolyte interface, leads to irreversible capacity loss [44]. In addition, the less decomposition of Li₂O can interrupt the disinsertion of Li⁺ ions during the first charging process [45, 46]. The specific capacities of NFO/C-350 are always higher than those of the other two samples, because the carbon matrix with appropriate carbon content can improve the conductivity of the material without causing too much resistance to the passage of Li⁺ ions. The lowest charge specific capacity of NFO/C-300 may be because the high carbon content increases the resistance of Li⁺ diffusion, resulting in the incomplete decomposition of Li₂O formed in the discharge process [47]. Besides, the high specific surface area of NFO/C-300 leads to more consumption of lithium to form the SEI film, resulting in a lower capacity obtained during the first charging process. Combined with the XRD results, it can be seen that the lower first discharge specific

capacity of NFO/C-400 can be attributed to the presence of Fe_{0.64}Ni_{0.36}, which makes less active NiFe₂O₄ material that can participate in the electrochemical reaction.

Figure 5b–d shows the charge and discharge profiles for several selected cycles of the samples. There is a clear difference in the curve distribution of the three samples. Among them, the discharge curve distribution of NFO/C-300 is the most sparse and the voltage platform changes the most. After the first cycle, NFO/C-350 shows higher charge and discharge specific capacities than the other two samples. Meantime, the charge/discharge curves can remain highly overlapped, indicating the excellent reversibility of redox reaction.

Figure 6a shows the cycling performances of NFO/C-300, NFO/C-350, and NFO/C-400 at 200 mA g⁻¹ in the voltage window of 0.005–3.0 V. All samples present good cycling performance due to the protective effect of the carbon matrix on the NiFe₂O₄ material, which can maintain the structural stability of NiFe₂O₄ during repeated charging and discharging. In addition, the nano-scaled particle size allows NiFe₂O₄ to undergo rapid and sufficient electrochemical reactions. The Coulombic efficiencies of the three materials remain above 99% after 20 cycles, indicating that the metal nanocrystals generated

Figure 6 **a** Cycling performance and **b** rate capability of NFO/C-300, NFO/C-350, and NFO/C-400.



during the discharge process are almost completely re-oxidized during the charging process so that the materials exhibit excellent reversibility.

The charge/discharge specific capacity of NFO/C-300 and NFO/C-350 shows a similar change trend. The capacity decreases in the initial 10 cycles, which may be related to the transformation between metal oxide and Fe and Ni metal nanocrystals, the generation and decomposition of Li_2O , and the volume expansion/contraction of metal oxide material. In the subsequent cycles, the capacity increases probably due to the gradual penetration of the electrolyte as the cycle progresses, which gradually activates the active sites after sufficient interfacial contact with the electrolyte. That is, the active nanoparticles involved in the electrochemical reaction gradually increase. Due to the high carbon content, there are fewer NiFe_2O_4 nanoparticles involved in the electrochemical reaction in NFO/C-300. Therefore, the discharge specific capacity of NFO/C-300 is significantly lower than that of the other two materials. Due to the protection of the carbon matrix and effective buffer of the volume change, NiFe_2O_4 particles inside NFO/C-350 have enough space to adapt to the volume change

and maintain structural stability to fully exert the capacity.

In Fig. 6a, the discharge specific capacity of NFO/C-400 decreases slowly and is lower than that of NFO/C-350, which can be attributed to their difference in carbon content and composition. Due to the lack of sufficient protection by carbon matrix, the active particles in NFO/C-400 cannot withstand repeated volume expansion and contraction, resulting in the gradual collapse of the structure and the gradual decline of capacity. The existence of $\text{Fe}_{0.64}\text{Ni}_{0.36}$ also has a negative effect on the electrochemical performance of NFO/C-400. As shown in Table 1, NFO/C-350 exhibits a higher reversible specific capacity after 200 cycles than the other two samples, indicating that the composite obtained at 350 °C has good cycling stability. In addition, compared with other reported anodes in Table S1, NiFe_2O_4 prepared in this work also shows certain competitive advantages in specific capacity and cycle stability.

Figure 6b presents the rate performance of the prepared electrodes at various current densities of 50, 100, 200, 300, 500, 800, 1000, and 100 mA g⁻¹. It can be seen that the discharge specific capacity of the

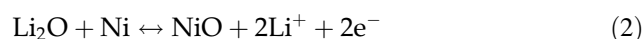
Table 1 Charge/discharge data of NFO/C-300, NFO/C-350, and NFO/C-400 in the first cycle and the 200th cycle

Sample	1st charge capacity (mAh g ⁻¹)	1st discharge capacity (mAh g ⁻¹)	1st coulombic efficiency (%)	200th charge capacity (mAh g ⁻¹)	200th discharge capacity (mAh g ⁻¹)	200th capacity retention (%)
NFO/C-300	441.3	1066.5	41.4	461.6	462.4	43.4
NFO/C-350	1004.6	1385.8	72.5	828.3	832.0	60.0
NFO/C-400	705.5	963.7	73.2	543.7	545.2	56.6

three samples decreases gradually with the increase in the current density, which is related to the polarization degree within the cell. As the current density gradually increases, the time for Li⁺ ions to pass through the carbon wall to participate in the electrochemical reaction with active particles is gradually shortened. A large amount of Li⁺ ions are rapidly transferred to the surface of the negative electrode, which reduces the Li⁺ concentration in the electrolyte, leading to concentration polarization. The increase in battery internal resistance makes the voltage quickly reach the cut-off voltage [18, 34]. The amount of NiFe₂O₄ that can participate in the electrochemical reaction gradually decreases with the increase in the current density, resulting in the lower specific capacity at higher rates. When the current density returns to 100 mA g⁻¹, all samples show stable and high specific capacity, which may be attributed to that the unique graded porous structure ensures the structural stability of the composite at high rates. In brief, NFO/C-350 exhibits satisfactory rate capability and excellent structural stability at high current densities.

Figure 7a shows the cyclic voltammetry curves (CV) of NFO/C-350 for the first three cycles at a scan rate of 0.2 mV s⁻¹, which provides a clear view of the electrochemical reaction potential. During the first scan, two cathodic peaks can be observed at 0.73 V and 0.21 V, corresponding to the formation of the SEI film and the reduction of NiFe₂O₄ to Ni and Fe according to Eq. (1) [41, 42]. The anodic peak at 1.85 V is attributed to the oxidation of Ni and Fe to NiO and Fe₂O₃ and the decomposition of Li₂O [48, 49], as illustrated in Eqs. (2) and (3). After the

first cycle, the CV curves overlap very well and the peak intensity of the oxidation and reduction peaks are close, implying that the NFO/C-350 electrode has good charge–discharge stability and cycling reversibility. Figure 8a illustrates the charge/discharge process of the composite with unique graded porous structure according to the following electrochemical reactions.



The electrochemical reaction kinetics behavior of the NFO/C-350 electrode has been evaluated based on the CV curves at different scan rates. Figure 7b shows the CV curves of the NFO/C-350 electrode at various rates from 0.1 to 2.0 mV s⁻¹. The CV curve still preserves its original shape well with the increase in scan rate. The degree of capacitive effect can be qualitatively analyzed by the relationship between the measured peak currents (*i*) and scan rates (*v*) in Eq. (4) [50]. The value of *b* can be determined by the slope in Eq. (5) [51], where *a* and *b* are adjustable parameters. When the value of *b* is 0.5, it indicates that the electrochemical reaction is a diffusion-controlled process. When the value of *b* is 1.0, it represents that the electrochemical reaction is a capacitive-controlled process. The *b* values corresponding to the cathodic peaks and the anodic peaks are 0.63 and 0.67 (Fig. 7c), respectively, indicating that the electrochemical process is controlled by both diffusion and capacitive behaviors. The percentages of capacitive contribution at different scan rates are

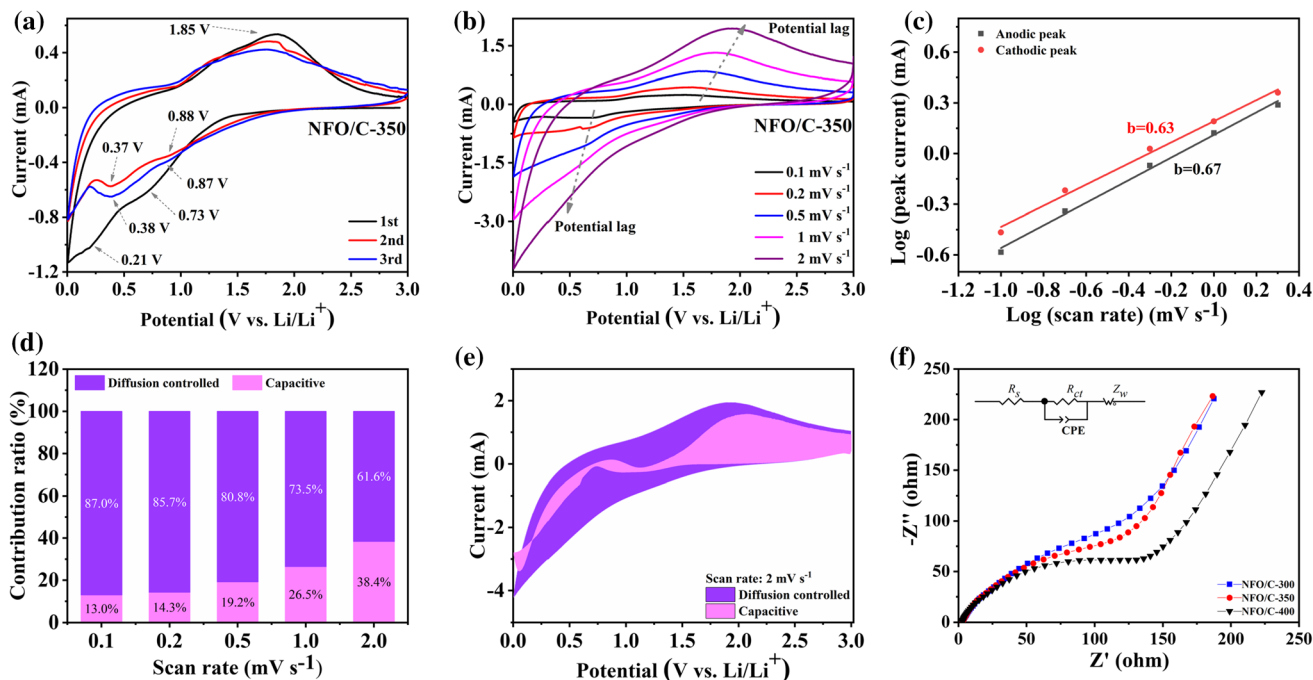
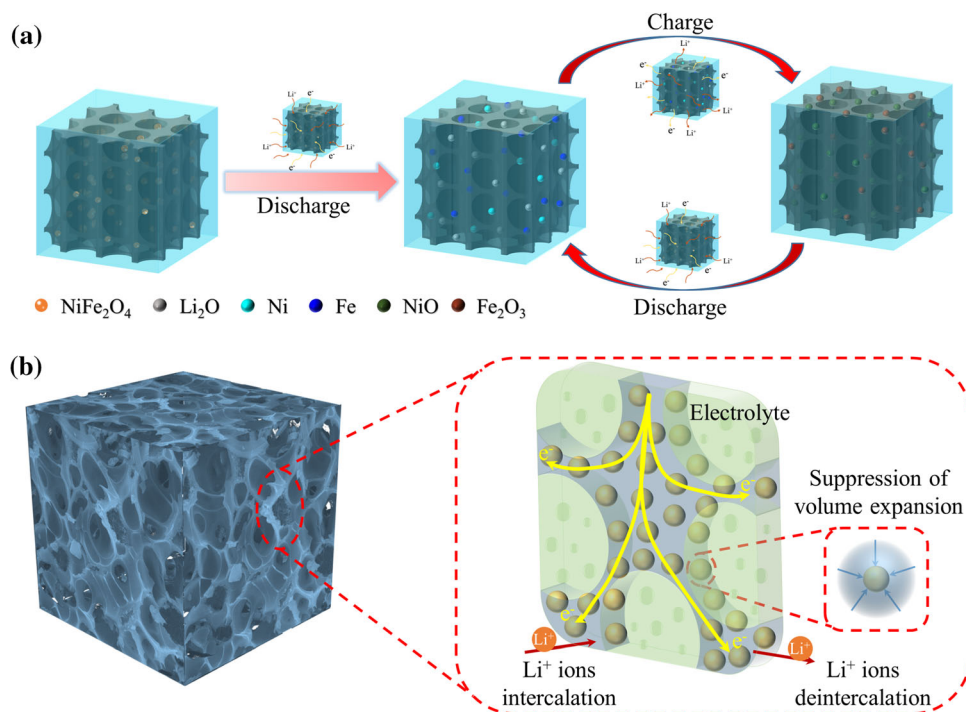


Figure 7 **a** First three CV curves at 0.2 mV s^{-1} ; **b** CV curves at various scan rates; **c** Relationship between log (peak current) and log (scan rate); **d** Separation of capacitive and diffusion

contribution at 0.1 mV s^{-1} ; **e** contribution ratio of capacitive at different scan rates for NFO/C-350; **f** EIS curves of the prepared electrodes (the inset is the equivalent circuit model).

Figure 8 **a** Illustration of the charge/discharge process and **b** mechanism illustration of the graded porous $\text{NiFe}_2\text{O}_4/\text{C}$ anode.



further calculated according to Eqs. (6) and (7) [52], where k_1v and $k_2v^{1/2}$ correspond to the capacitive contribution and diffusion contribution, respectively. As shown in Fig. 7d, the capacitive contribution ratio

increases with the increase in scan rate. The capacitive contribution ratio of the NFO/C-350 electrode at 2 mV s^{-1} is 38.4%. The high capacitive contribution ratio may be attributed to the high specific surface

area and large porosity of NFO/C-350, which can provide more electrochemical active sites and promote fast charge storage.

$$i = av^b \quad (4)$$

$$\log i = b \log v + \log a \quad (5)$$

$$i = k_1v + k_2v^{1/2} \quad (6)$$

$$i/v^{1/2} = k_1v^{1/2} + k_2 \quad (7)$$

EIS curves of the prepared electrodes are investigated and fitted in order to better understand and interpret the charge transfer kinetics. As shown in Fig. 7f, the three samples show typical Nyquist plots that are consisted of a semicircular arc at medium-high frequency and a slope line at low frequency. The intercept of semicircular arc at the real axis of impedance (Z') indicates the ohmic resistance (R_s) of the electrolyte. The semicircular arc at the middle-high frequency region corresponds to the charge-transfer impedance (R_{ct}) at the electrode/electrolyte interface. The slope line at the low frequency region is attributed to the Warburg impedance (Z_w), which is related to Li^+ ions diffusion in the solid phase. NFO/C-350 exhibits a lower charge transfer resistance than the other two samples, indicating the fast charge transfer rate.

As illustrated in Fig. 8b, three factors are conducive to the excellent electrochemical performances of the $\text{NiFe}_2\text{O}_4/\text{C}$ composite. Firstly, NiFe_2O_4 nanoparticles are perfectly wrapped by the carbon matrix. The unique interconnection and porous structure of carbon matrix not only improve the electronic conductivity, but also provide sufficient space to accommodate the volume change of NiFe_2O_4 during cycling. Secondly, the graded porous structure can help the infiltration of the electrolyte, increase the interfacial contact area between electrolyte and electrode material, and provide sufficient space to accommodate volume change. Finally, the active nanomaterials without agglomeration can shorten the transmission distance of electrons and ions and ensure the utilization efficiency of active particles. In short, the synergistic effect of these factors makes the composite with the special structure prepared in this study plays an outstanding electrochemical performance.

Conclusion

In summary, graded porous structure of $\text{NiFe}_2\text{O}_4/\text{C}$ anode material has been successfully in situ constructed by a low-temperature combustion method. As the calcination temperature increases, impurity phase appears in the product and the particle size of NiFe_2O_4 gradually increases. $\text{NiFe}_2\text{O}_4/\text{C}$ obtained at 350 °C shows excellent electrochemical performance, including a high first discharge specific capacity of 1385.8 mAh g^{-1} with high initial Coulombic efficiency of 72.5% and a high reversible capacity of 832 mAh g^{-1} at 200 mA g^{-1} after 200 cycles. The unique graded porous structure has a positive effect on the electrochemical performance of $\text{NiFe}_2\text{O}_4/\text{C}$. The simultaneous existence of carbon matrix, active nanoparticles, and graded porous structure improves the electrical conductivity of $\text{NiFe}_2\text{O}_4/\text{C}$ electrode, promotes the transport kinetics of Li^+ ions and electrons, provides large electrode/electrolyte interfacial contact area, buffers the surface stress caused by the volume change of metal oxide during cycling, and maintains the structural stability of the material, so as to realize high capacity, excellent cycle stability, and superior rate performance. Considering that other metal oxides also suffer from unsatisfactory electrochemical performance due to low electronic conductivity and huge volume expansion/contraction during cycling, this work can provide an effective route for the design and preparation of other similar metal oxides.

Acknowledgements

This work was supported by the National Natural Science Foundation of China (51902213) and Natural Science Foundation of Hebei Education Department (BJ2020046).

Supplementary Information: The online version contains supplementary material available at <http://doi.org/10.1007/s10853-022-07576-z>.

References

- [1] Weng Y-T, Liu H-W, Pei A, Shi F, Wang H, Lin C-Y, Huang S-S, Su L-Y, Hsu J-P, Fang C-C, Cui Y, Wu N-L (2019) An

- ultrathin ionomer interphase for high efficiency lithium anode in carbonate based electrolyte. *Nat Commun* 10:5824. <https://doi.org/10.1038/s41467-019-13783-1>
- [2] Liu X, Liu F, Yu J, Xiong G, Zhao L, Sang Y, Zuo S, Zhang J, Liu H, Zhou W (2020) Charge redistribution caused by S, P synergistically active Ru endows an ultrahigh hydrogen evolution activity of S-doped RuP embedded in N, P, S-doped carbon. *Adv Sci* 7:2001526. <https://doi.org/10.1002/advs.202001526>
- [3] Mufutau Opeyemi B (2021) Path to sustainable energy consumption: the possibility of substituting renewable energy for non-renewable energy. *Energy* 228:120519. <https://doi.org/10.1016/j.energy.2021.120519>
- [4] Aslam MK, Hussain T, Tabassum H, Wei Z, Tang W, Li S, Bao S-j, Zhao XS, Xu M (2022) Sulfur encapsulation into yolk-shell Fe₂N@nitrogen doped carbon for ambient-temperature sodium-sulfur battery cathode. *Chem Eng J* 429:132389. <https://doi.org/10.1016/j.cej.2021.132389>
- [5] Li S, Xiang Q, Aslam MK, Cen Y, Guo C, Hu J, Li W, Chen C (2019) Fe-functionalized mesoporous carbonaceous microsphere with high sulfur loading as cathode for lithium-sulfur batteries. *J Electroanal Chem* 850:113408. <https://doi.org/10.1016/j.jelechem.2019.113408>
- [6] Park JY, Kim SJ, Yim K, Dae KS, Lee Y, Dao KP, Park JS, Jeong HB, Chang JH, Seo HK, Ahn CW, Yuk JM (2019) Pulverization-tolerance and capacity recovery of copper sulfide for high-performance sodium storage. *Adv Sci* 6:1900264. <https://doi.org/10.1002/advs.201900264>
- [7] Gozdur R, Guzowski B, Dimitrova Z, Noury A, Mitukiewicz G, Batory D (2021) An energy balance evaluation in lithium-ion battery module under high temperature operation. *Energy Convers Manag* 227:113565. <https://doi.org/10.1016/j.enconman.2020.113565>
- [8] Liu Z, Wang C, Guo X, Cheng S, Gao Y, Wang R, Sun Y, Yan P (2021) Thermal characteristics of ultrahigh power density lithium-ion battery. *J Power Sources* 506:230205. <https://doi.org/10.1016/j.jpowsour.2021.230205>
- [9] Mostafavi A, Jain A (2021) Dual-purpose thermal management of Li-ion cells using solid-state thermoelectric elements. *Int J Energy Res* 45:4303–4313. <https://doi.org/10.1002/er.6094>
- [10] Chen T, Mu D, Li R, Liu J, Ma Q, Ding F, Dai C (2019) Synthesis of metal–organic sulfides as anode materials for lithium-ion batteries at room temperature. *Energy Technol* 7:1800889. <https://doi.org/10.1002/ente.201800889>
- [11] Zhao E, Zhao S, Wu X, Li J, Yu L, Nan C, Cao G (2019) Electrochemical performance of Li₂O–V₂O₅–SiO₂–B₂O₃ glass as cathode material for lithium ion batteries. *J Materomics* 5:663–669. <https://doi.org/10.1016/j.jmat.2019.05.002>
- [12] Hua X, Eggeman AS, Castillo-Martínez E, Robert R, Geddes HS, Lu Z, Pickard CJ, Meng W, Wiaderek KM, Pereira N, Amatucci GG, Midgley PA, Chapman KW, Steiner U, Goodwin AL, Grey CP (2021) Revisiting metal fluorides as lithium-ion battery cathodes. *Nat Mater* 20:841–850. <https://doi.org/10.1038/s41563-020-00893-1>
- [13] Nakajima K, Souza FL, Freitas ALM, Thron A, Castro RHR (2021) Improving thermodynamic stability of nano-LiMn₂O₄ for Li-ion battery cathode. *Chem Mater* 33:3915–3925. <https://doi.org/10.1021/acs.chemmater.0c04305>
- [14] Okubo M, Ko S, Dwibedi D, Yamada A (2021) Designing positive electrodes with high energy density for lithium-ion batteries. *J Mater Chem A* 9:7407–7421. <https://doi.org/10.1039/D0TA10252K>
- [15] Rivera-Lugo Y, Félix-Navarro R, Trujillo-Navarrete B, Reynoso-Soto E, Silva-Carrillo C, Cruz-Gutiérrez C, Quiróga-González E, Calva-Yáñez J (2021) Flower-like δ-MnO₂ as cathode material of Li-ion batteries of high charge-discharge rates. *Fuel* 287:119463. <https://doi.org/10.1016/j.fuel.2020.119463>
- [16] Mo R, Tan X, Li F, Tao R, Xu J, Kong D, Wang Z, Xu B, Wang X, Wang C, Li J, Peng Y, Lu Y (2020) Tin-graphene tubes as anodes for lithium-ion batteries with high volumetric and gravimetric energy densities. *Nat Commun* 11:1374. <https://doi.org/10.1038/s41467-020-14859-z>
- [17] Collins GA, Geaney H, Ryan KM (2021) Alternative anodes for low temperature lithium-ion batteries. *J Mater Chem A* 9:14172–14213. <https://doi.org/10.1039/D1TA00998B>
- [18] Feng D, Yang H, Guo X (2019) 3-Dimensional hierarchically porous ZnFe₂O₄/C composites with stable performance as anode materials for Li-ion batteries. *Chem Eng J* 355:687–696. <https://doi.org/10.1016/j.cej.2018.08.202>
- [19] Li Y, Meng Y, Liu X, Xiao M, Hu Q, Li R, Ke X, Ren G, Zhu F (2019) Double-protected zinc ferrite nanospheres as high rate and stable anode materials for lithium ion batteries. *J Power Sources* 442:227256. <https://doi.org/10.1016/j.jpowsour.2019.227256>
- [20] Xiao Y, Zhang Z, Ma Z, Zhang G, Feng C (2021) Synthesis and electrochemical properties of ZnFe₂O₄/C as novel anode material for lithium ion battery. *Ionics* 27:1377–1384. <https://doi.org/10.1007/s11581-021-03931-3>
- [21] Zhao T, Ji R, Meng Y (2021) Foamed porous structure Fe-Mn oxides/C composites as novel anode materials of lithium-ion batteries. *J Alloys Compd* 882:160643. <https://doi.org/10.1016/j.jallcom.2021.160643>
- [22] Aslam MK, Javed MS, Hussain S, Xu J, Chen C (2018) Facile synthesis of cobalt ferrite nanoparticles (CFO-NPs) as anode material with enhanced lithium storage capability. *Mater Sci Eng B* 236–237:162–169. <https://doi.org/10.1016/j.mseb.2018.11.019>

- [23] Aslam MK, Shah SSA, Najam T, Li S, Chen C (2019) Decoration of cobalt/iron oxide nanoparticles on N-doped carbon nanosheets: Electrochemical performances for lithium-ion batteries. *J Appl Electrochem* 49:433–442. <https://doi.org/10.1007/s10800-019-01291-5>
- [24] Li Z, Qiao N, Nie J, Zhao J, Wang J, Feng X, Yao S (2020) NiO/NiFe₂O₄ nanocubes derived from Prussian blue as anode materials for Li-ion batteries. *Mater Lett* 275:128077. <https://doi.org/10.1016/j.matlet.2020.128077>
- [25] Wang Z, Zhang X, Liu X, Zhang W, Zhang Y, Li Y, Qin C, Zhao W, Bakenov Z (2020) Dual-network nanoporous NiFe₂O₄/NiO composites for high performance Li-ion battery anodes. *Chem Eng J* 388:124207. <https://doi.org/10.1016/j.cej.2020.124207>
- [26] Shen H, Xia X, Yan S, Jiao X, Sun D, Lei W, Hao Q (2021) SnO₂/NiFe₂O₄/graphene nanocomposites as anode materials for lithium ion batteries. *J Alloys Compd* 853:157017. <https://doi.org/10.1016/j.jallcom.2020.157017>
- [27] Lei X, Li Y, Weng C, Liu Y, Liu W, Hu J, Yang C, Lin Z, Liu M (2020) Construction of heterostructured NiFe₂O₄-C nanorods by transition metal recycling from simulated electroplating sludge leaching solution for high performance lithium ion batteries. *Nanoscale* 12:13398–13406. <https://doi.org/10.1039/d0nr02290j>
- [28] Bao S, Xiao Y, Li J, Yue B, Li Y, Sun W, Liu L, Huang Y, Wang L, Zhang P, Lai X (2020) Coral-like NiFe₂O₄/C composite as the high-performance anode material for lithium-ion batteries. *Electron Mater Lett* 16:207–215. <https://doi.org/10.1007/s13391-020-00207-2>
- [29] Cheng R (2020) NiFe₂O₄-coated activated carbon composite as a cathode material for lithium–sulfur batteries. *Int J Electrochem Sci* 15:2624–2633. <https://doi.org/10.20964/20.03.33>
- [30] Zou Y, Li Z, Liu Y, Duan J, Long B (2020) Coaxial structure of NiFe₂O₄/CNTs composites as anodes for enhanced lithium ion batteries. *J Alloys Compd* 820:153085. <https://doi.org/10.1016/j.jallcom.2019.153085>
- [31] Jin R, Jiang H, Sun Y, Ma Y, Li H, Chen G (2016) Fabrication of NiFe₂O₄/C hollow spheres constructed by mesoporous nanospheres for high-performance lithium-ion batteries. *Chem Eng J* 303:501–510. <https://doi.org/10.1016/j.cej.2016.06.032>
- [32] Zhang Y, Cao W, Cai Y, Shu J, Cao M (2019) Rational design of NiFe₂O₄-rGO by tuning the compositional chemistry and its enhanced performance for a Li-ion battery anode. *Inorg Chem Front* 6:961–968. <https://doi.org/10.1039/C9QI00055K>
- [33] Dong T, Liu Y, Liu D, Yang P (2018) NiFe₂O₄ nanofibers: morphology, lithium storage and photocatalytic properties. *J Nanosci Nanotechnol* 18:2758–2765. <https://doi.org/10.1166/jnn.2018.14299>
- [34] Wu F, Huang R, Mu D, Wu B, Chen S (2014) New synthesis of a foam like Fe₃O₄/C composite via a self-expanding process and its electrochemical performance as anode material for lithium-ion batteries. *ACS Appl Mater Interfaces* 6:19254–19264. <https://doi.org/10.1021/am505290f>
- [35] Zeng Z, Zhao H, Wang J, Lv P, Zhang T, Xia Q (2014) Nanostructured Fe₃O₄@C as anode material for lithium-ion batteries. *J Power Sources* 248:15–21. <https://doi.org/10.1016/j.jpowsour.2013.09.063>
- [36] Dong T, Wang G, Yang P (2017) Electrospun NiFe₂O₄@C fibers as high-performance anode for lithium-ion batteries. *Diam Relat Mater* 73:210–217. <https://doi.org/10.1016/j.diamond.2016.09.024>
- [37] Liu X, Li X, Sun Y, Zhang S, Wu Y (2019) Onion-like carbon coated Fe₃C nanocapsules embedded in porous carbon for the stable lithium-ion battery anode. *Appl Surf Sci* 479:318–325. <https://doi.org/10.1016/j.apsusc.2019.02.098>
- [38] Xu Y, Fan Y, Tian X, Liang Q, Liu X, Sun Y (2020) p-p heterojunction composite of NiFe₂O₄ nanoparticles-decorated NiO nanosheets for acetone gas detection. *Mater Lett* 270:127728. <https://doi.org/10.1016/j.matlet.2020.127728>
- [39] Yao L, Cao W, Zhao J, Zheng Q, Wang Y, Jiang S, Pan Q, Song J, Zhu Y, Cao M (2022) Regulating bifunctional flower-like NiFe₂O₄/graphene for green EMI shielding and lithium ion storage. *J Mater Sci Technol* 127:48–60. <https://doi.org/10.1016/j.jmst.2022.04.010>
- [40] Xie Q, Song R, Zhao P, Zhang Y, Wu S, Xie D (2018) In-plane porous Co₃O₄ nanosheet assembled 3D hierarchical clusters grown on stainless steel mesh as binder-free anodes for high performance lithium ion batteries. *J Mater Chem A* 6:8388–8395. <https://doi.org/10.1039/c8ta00068a>
- [41] Vidal-Abarca C, Lavela P, Tirado JL (2010) The origin of capacity fading in NiFe₂O₄ conversion electrodes for lithium ion batteries unfolded by ⁵⁷Fe Mössbauer spectroscopy. *J Phys Chem C* 114:12828–12832. <https://doi.org/10.1021/jp103888a>
- [42] Fu Y, Wan Y, Xia H, Wang X (2012) Nickel ferrite–graphene heteroarchitectures: toward high-performance anode materials for lithium-ion batteries. *J Power Sources* 213:338–342. <https://doi.org/10.1016/j.jpowsour.2012.04.039>
- [43] Huang XH, Tu JP, Zhang B, Zhang CQ, Li Y, Yuan YF, Wu HM (2006) Electrochemical properties of NiO–Ni nanocomposite as anode material for lithium ion batteries. *J Power Sources* 161:541–544. <https://doi.org/10.1016/j.jpowsour.2006.03.039>
- [44] Peled E, Menkin S (2017) Review—SEI: past, present and future. *J Electrochem Soc* 164:A1703–A1719. <https://doi.org/10.1149/2.1441707jes>

- [45] Deshpande R, Verbrugge M, Cheng Y-T, Wang J, Liu P (2012) Battery cycle life prediction with coupled chemical degradation and fatigue mechanics. *J Electrochem Soc* 159:A1730–A1738. <https://doi.org/10.1149/2.049210jes>
- [46] Kang Y-M, Kim K-T, Lee K-Y, Lee S-J, Jung J-H, Lee J-Y (2003) Improvement of initial coulombic efficiency of Co_3O_4 by ballmilling using Ni as an additive. *J Electrochem Soc* 150:A1538. <https://doi.org/10.1149/1.1617299>
- [47] Han D, Song G, Liu B, Yan H (2015) Core-shell-structured nickel ferrite/onion-like carbon nanocapsules: an anode material with enhanced electrochemical performance for lithium-ion batteries. *RSC Adv* 5:42875–42880. <https://doi.org/10.1039/c5ra05101k>
- [48] Lavela P, Tirado JL (2007) CoFe_2O_4 and NiFe_2O_4 synthesized by sol-gel procedures for their use as anode materials for Li ion batteries. *J Power Sources* 172:379–387. <https://doi.org/10.1016/j.jpowsour.2007.07.055>
- [49] Ding Y, Yang Y, Shao H (2013) One-pot synthesis of $\text{NiFe}_2\text{O}_4/\text{C}$ composite as an anode material for lithium-ion batteries. *J Power Sources* 244:610–613. <https://doi.org/10.1016/j.jpowsour.2013.01.043>
- [50] Huang Y, Li Y, Huang R, Ji J, Yao J, Xiao S (2021) One-pot hydrothermal synthesis of N-rGO supported Fe_2O_3 nanoparticles as a superior anode material for lithium-ion batteries. *Solid State Ionics* 368:115693. <https://doi.org/10.1016/j.ssi.2021.115693>
- [51.] Qi M, Lin L, Wang L, Bai Z, Yu Y, Gu J, Liu Y (2021) Spindle MnCO_3 tightly encapsulated by MXene nanoflakes with strengthened interface effect for lithium-ion battery. *Surf Coat Technol* 417:127192. <https://doi.org/10.1016/j.surfcoat.2021.127192>
- [52] Yan S, Luo S, Liu H, Yang L, Wang Q, Zhang Y, Liu X (2022) In-situ partial reduction-sulfurized $\text{Fe}_3\text{O}_4@/\text{FeS}$ based on pickling iron red as a versatile electrode for high-performance lithium ion batteries and supercapacitor devices. *Surf Coat Technol* 429:127980. <https://doi.org/10.1016/j.surfcoat.2021.127980>

Publisher's Note Springer Nature remains neutral with regard to jurisdictional claims in published maps and institutional affiliations.

Springer Nature or its licensor holds exclusive rights to this article under a publishing agreement with the author(s) or other rightsholder(s); author self-archiving of the accepted manuscript version of this article is solely governed by the terms of such publishing agreement and applicable law.